

PAPER • OPEN ACCESS

# Structural distortion and dynamical electron correlation driven enhanced ferromagnetism in Ni-doped two-dimensional $\text{Fe}_5\text{GeTe}_2$ beyond room temperature

To cite this article: Sukanya Ghosh *et al* 2024 *2D Mater.* **11** 035002

View the [article online](#) for updates and enhancements.

You may also like

- [First principles study of electronic structure and transport in graphene grain boundaries](#)  
Aleksander Bach Lorentzen, Fei Gao, Peter Bøggild *et al.*
- [Symmetry classification of 2D materials: layer groups versus space groups](#)  
Jingheng Fu, Mikael Kuisma, Ask Hjorth Larsen *et al.*
- [High spin-Chern-number insulator in -antimonene with a hidden topological phase](#)  
Baokai Wang, Xiaoting Zhou, Yi-Chun Hung *et al.*



## PAPER

## OPEN ACCESS

RECEIVED  
10 December 2023REVISED  
14 March 2024ACCEPTED FOR PUBLICATION  
5 April 2024PUBLISHED  
15 April 2024

Original Content from  
this work may be used  
under the terms of the  
[Creative Commons  
Attribution 4.0 licence](#).

Any further distribution  
of this work must  
maintain attribution to  
the author(s) and the title  
of the work, journal  
citation and DOI.



# Structural distortion and dynamical electron correlation driven enhanced ferromagnetism in Ni-doped two-dimensional $\text{Fe}_5\text{GeTe}_2$ beyond room temperature

Sukanya Ghosh , Soheil Ershadrad and Biplab Sanyal\*

Department of Physics and Astronomy, Uppsala University, Box-516, 75120 Uppsala, Sweden

\* Author to whom any correspondence should be addressed.

E-mail: [biplab.sanyal@physics.uu.se](mailto:biplab.sanyal@physics.uu.se)**Keywords:** two-dimensional magnets, Ni-doped  $\text{Fe}_5\text{GeTe}_2$ , electron correlation, first-principles calculations, dynamical mean field theory, exchange interactions, Curie temperatureSupplementary material for this article is available [online](#)

## Abstract

Achieving beyond room-temperature ferromagnetism in two-dimensional (2D) magnets is immensely desirable for spintronic applications.  $\text{Fe}_5\text{GeTe}_2$  is an exceptional van der Waals metallic ferromagnet due to its tunable physical properties and relatively higher Curie temperature ( $T_C$ ) than other 2D magnets. Using density functional theory combined with dynamical electron correlation and Monte Carlo simulations, we find the  $T_C$  of  $(\text{Fe}_{1-\delta}\text{Ni}_\delta)_5\text{GeTe}_2$  monolayer can increase up to  $\sim 400$  K at  $\delta \sim 0.20$  ( $\delta$ : fractional occupation). Two specific Fe sublattices are identified to be the most energetically preferred sites to host Ni. Exchange interactions between particular Fe pairs play a dominating role in controlling  $T_C$ , influenced by the dopant-induced structural distortions. Dynamical electron correlation induces site- and orbital-specific quasi-particle mass of Fe- $d$  states with varying Ni concentrations. This work provides fundamental insights into 2D magnetism as an interplay of structural and electronic aspects and would guide to tailoring exciting magnetic phenomena in similar systems.

## 1. Introduction

Atomically thin, layered quasi-two-dimensional (2D) van der Waals (vdW) crystals exhibit exceptional physical properties [1, 2]. Regarding 2D magnets, however, according to the Mermin–Wagner theorem, an intrinsic long-range magnetic order can not exist in the isotropic 2D limit because strong thermal fluctuations prohibit continuous symmetries to break spontaneously [3]. The presence of weak magnetic anisotropy is sufficient to open up a sizable gap in the magnon spectra, causing long-range magnetic order to persist in materials with the spatial dimension  $D \leq 2$  at a finite temperature. In the 2D magnets, i.e. when the system is periodic along any two directions in space, the crossover from Heisenberg to Ising-like behavior depends on the strength of both exchange interactions and magnetic anisotropy [4].

In recent times, the 2D or quasi-2D vdW materials, for example,  $\text{Cr}_2\text{Ge}_2\text{Te}_6$  [5–7],  $\text{CrI}_3$  [8–12],  $\text{CrTe}_2$  [13] etc have constituted a rich platform

to explore low-dimensional magnetism from the aspects of fundamental understanding as well as for demands in technological purposes [1, 2, 14]. The tunable physical properties of this class of systems make them more interesting and useful for practical applications [1, 5–12, 14, 15]. Among the newly discovered vdW magnetic materials metallic  $\text{Fe}_n\text{GeTe}_2$  ( $n = 3, 4, 5$ ) systems, commonly referred to as FGT are quite special for their exotic structural, electronic and magnetic properties as reported in recent studies [16–20]. Ferromagnetism close to the room temperature increases their demand for spintronic applications. Among different FGT systems,  $\text{Fe}_3\text{GeTe}_2$  has been mostly studied so far. Recent studies show it is possible to increase the transition temperature of  $\text{Fe}_3\text{GeTe}_2$  by applying external perturbations, e.g. pressure [21, 22], gating [23, 24], carrier doping [25] etc.

Intercalation of more Fe atoms into  $\text{Fe}_3\text{GeTe}_2$  increases the Curie temperature ( $T_C$ ), for example,  $\text{Fe}_5\text{GeTe}_2$  exhibits ferromagnetism close to room

temperature (275–310 K) [18, 26, 27]. High  $T_C$  makes  $\text{Fe}_5\text{GeTe}_2$  more advantageous for potential room-temperature spintronic applications. It has also been found that substitutional doping of  $\text{Fe}_5\text{GeTe}_2$  with cobalt increases the magnetic ordering temperature to  $\sim 360$  K influencing the magnetic ground state, easy axis of anisotropy, interlayer stacking and magnetic textures [28–31]. A recent study by Chen *et al* has reported an enhancement of ferromagnetism in bulk  $\text{Fe}_5\text{GeTe}_2$  up to 478 K with Ni doping [19]. This study shows that Ni doping increases the  $T_C$  beyond room temperature up to a certain doping concentration followed by a decrease. The scanning tunnelling electron microscopy images show ruffled configurations of  $(\text{Fe}_{1-\delta}\text{Ni}_\delta)_5\text{GeTe}_2$  ( $\delta$ : doping concentration) for higher concentrations of Ni doping. The alteration in structural, electronic and magnetic properties of  $(\text{Fe}_{1-\delta}\text{Ni}_\delta)_5\text{GeTe}_2$  with Ni doping demands a thorough investigation.

It is known that the FGT systems are special for their site-dependent electronic and magnetic properties [17, 22, 32]. Reports from the literature indicate the admixture of localized and itinerant electronic states in these systems [32–34]. In a previous study, we have shown that the inclusion of the dynamical electron correlation effects is important to correctly identify their electronic and magnetic behavior [17]. Specifically, it was demonstrated that density functional theory in conjunction with dynamical mean field theory (DFT+DMFT) is the most accurate approach to correctly describe the physical properties of these systems, e.g. spectral features, effective mass, and Sommerfeld coefficient [17].

Experimentally it has been observed that the magnetism of  $\text{Fe}_5\text{GeTe}_2$  system can be tuned by substitutional doping with Ni. The  $T_C$  of Ni-doped  $\text{Fe}_5\text{GeTe}_2$  first increases with doping and then reduces above a certain Ni concentration [19]. Such behavior of  $T_C$  as a function of Ni doping is highly non-trivial which demands significant microscopic understanding from advanced theories. This recent experimental observation by Chen *et al* has motivated us to investigate the behavior of  $T_C$  with Ni doping.  $\text{Fe}_5\text{GeTe}_2$  exhibits peculiar structural magnetic properties compared to other FGT systems. One particular Fe sublattice, situated directly above or below Ge, is responsible for the magnetic peculiarities present in this system. Our recent study on pristine  $\text{Fe}_5\text{GeTe}_2$  explains the experimentally observed unusual structural and magnetic behavior of this system [17]. Therefore, another motivation of our present study is to investigate how substitutional doping with Ni alters the structural, electronic and magnetic properties of Ni-doped  $\text{Fe}_5\text{GeTe}_2$  or  $(\text{Fe}_{1-\delta}\text{Ni}_\delta)_5\text{GeTe}_2$ .

For the application of room-temperature spintronic devices, it is necessary to find materials with a higher  $T_C$ . The  $(\text{Fe}_{1-\delta}\text{Ni}_\delta)_5\text{GeTe}_2$  system

is an extremely rare example of strongly enhanced ferromagnetism. In addition, this system offers unique or alternative avenues toward enhanced coercivity and can be a potential candidate for skyrmionics [19]. In addition to spintronic applications,  $(\text{Fe}_{1-\delta}\text{Ni}_\delta)_5\text{GeTe}_2$  also shows excellent properties in the field of energy conversion, e.g. oxygen evolution reaction [35].

In this work, we investigate the mechanisms responsible for the enhancement of  $T_C$  well above room temperature by substitutional doping with Ni in  $\text{Fe}_5\text{GeTe}_2$  monolayer. Our study reveals which particular Fe sites are more prone to host Ni dopant. Using DFT+DMFT, we explain how the tuning of exchange interactions between certain Fe pairs, caused by structural modifications, plays the dominating role in increasing  $T_C$  up to a certain doping. Reduction in  $T_C$  for higher doping is caused by the replacement of magnetic Fe atom by nonmagnetic Ni, however, the dominating exchange remains ferromagnetic (FM), as observed in the experiment [19], but in contrast with a recent DFT study [36]. Our DFT+DMFT study shows the strength of electron correlation for different Fe sublattices varies with doping concentration. In addition to pristine  $\text{Fe}_5\text{GeTe}_2$  [17], the site-dependence of effective mass is present in  $(\text{Fe}_{1-\delta}\text{Ni}_\delta)_5\text{GeTe}_2$  as well. We have also investigated how the magnetic anisotropy energy and spectral properties of  $(\text{Fe}_{1-\delta}\text{Ni}_\delta)_5\text{GeTe}_2$  get modified with substitutional doping.

## 2. Computational methodology

### 2.1. Geometry optimization

Geometry optimizations of  $(\text{Fe}_{1-\delta}\text{Ni}_\delta)_5\text{GeTe}_2$  monolayer are performed using the Vienna *Ab initio* Simulation Package [37, 38]. The generalized gradient approximation (GGA) has been used to treat the exchange-correlation interactions within the Perdew–Burke–Ernzerhof form [39].  $18 \times 18 \times 1$  Monkhorst–Pack  $k$ -point mesh is used in our calculations for Brillouin zone integration [40]. To reduce the interaction between periodic images of the supercell along the  $z$ -axis a vacuum region of dimension  $20 \text{ \AA}$  is added perpendicular to the surface of monolayers. The unit cell parameters and atomic coordinates are optimized by the energy minimization technique based on the conjugate gradient algorithm with a force component tolerance of  $0.01 \text{ eV \AA}^{-1}$  on each atom. In our calculations, the energy cutoff for the plane-wave basis set is considered to be 500 eV.

### 2.2. DMFT

The main idea of DMFT is to replace the many-body lattice model with an effective Anderson impurity model. In this method, the entire lattice gets transformed into a simple problem where a single atom is

embedded in an electronic bath. This way, each lattice site is coupled with the rest of the crystal which is represented as the bath. Electrons on the single site could be created or annihilated by interacting with the bath. This impurity model offers an intuitive picture of the local quantum (temporal) fluctuations of a quantum many-body system [41].

The full-potential linear muffin-tin orbital (FP-LMTO) method, implemented in the RSPt code [42] is used to study the magnetic and electronic properties of  $(\text{Fe}_{1-\delta}\text{Ni}_\delta)_5\text{GeTe}_2$  monolayers. First, we perform standard DFT calculations, then the charge-self-consistent DMFT calculations are started from the converged DFT calculations using the RSPt code [42, 43]. To solve the effective impurity problem arising in the DMFT cycle we use the spin-polarized T-matrix fluctuation-exchange (SPTF) solver [44]. The double counting correction is considered as the orbitally averaged static part of the self-energy, which is usually done for the SPTF solver [44]. The effective Hubbard  $U$  parameter or  $U_{\text{eff}} = U - J_{\text{H}}$  ( $J_{\text{H}}$  is the Hund's exchange) for each Fe sublattice is obtained from the constrained linear response method (cLR) [17]. We use the  $U_{\text{eff}}$  values of 4.6, 4.1, 4.1, 4.6, 4.0, 3.7 and 6.8 for Fe5, Fe4, Fe3, Fe2, Fe1D, Fe1U and Ni, respectively, obtained from cLR.

### 2.3. Calculation of exchange interactions

The isotropic symmetric exchange interactions  $J_{ij}$  are computed within the full-potential linearized muffin-tin orbital basis implemented in the RSPt code. The Löwdin orthonormalized LMTO basis functions with long decaying tails are considered, which are more physical for metallic systems like  $\text{Fe}_5\text{GeTe}_2$  [45]. The Löwdin orbitals used in our calculations have been constructed from the original LMTO basis functions performing a  $k$ -point-wise orthonormalization.

The  $J_{ij}$  couplings are computed using force-theorem based Green's function formalism. The intersite exchange parameters are calculated using equation (1):

$$J_{ij} = \frac{T}{4} \sum_n \left[ \hat{\Delta}_i(i\omega_n) \hat{G}_{ij}^\uparrow(i\omega_n) \hat{\Delta}_j(i\omega_n) \hat{G}_{ji}^\downarrow(i\omega_n) \right], \quad (1)$$

where  $\Delta_i$  and  $\hat{G}_{ij}$  are the onsite spin splitting and the spin-dependent intersite Green's function, respectively. The trace in equation (1) is over the orbital degrees of freedom.  $\omega_n = 2\pi T(2n + 1)$  and  $T$  are the  $n$ th fermionic Matsubara frequency and the temperature, respectively. The onsite exchange splitting term  $\Delta_i$  includes the self-energy, which is given by:

$$\Delta_i(i\omega_n) = H_{\text{KS}}^\uparrow + \Sigma_i^\uparrow(i\omega_n) - H_{\text{KS}}^\downarrow - \Sigma_i^\downarrow(i\omega_n), \quad (2)$$

where  $H_{\text{KS}}$  and  $\Sigma_i$  are the Kohn–Sham Hamiltonian and site-dependent self-energy. The self-energy is obtained by solving the DMFT equations. In DMFT

calculations, The frequency-dependent self-energy is obtained from DMFT. The exchange splitting also depends on the frequency [45].

In the fully-relativistic case the generalized Heisenberg model becomes:

$$H = - \sum_{i \neq j} e_i^\alpha J_{ij} e_j^\beta, \quad (3)$$

where  $\alpha, \beta = x, y, z$ . The magnetic exchange parameters  $J_{ij}$  are  $(3 \times 3)$  tensors in the considered fully-relativistic case, which is a generalization of the  $J_{ij}$  scalar parameters [45]. To calculate the magnetic exchange interactions we use  $21 \times 21 \times 1$   $k$ -point mesh.

### 2.4. Magnetic anisotropy

The magnetic anisotropy is estimated based on the one-shot fully-relativistic calculations for the spin axis pointing along the  $x, y$ , and  $z$  directions. These calculations are run starting from the fully-converged self-consistent non-relativistic electronic structure. The value of anisotropy is obtained from the difference in the sum of the energy eigenvalues for the three spin directions, as already mentioned. Note that, this approach, which is based on the force theorem, often is a more accurate way of determining the magnetic anisotropy, compared to relativistic total energies [46]. We use the  $k$ -point grids with dimensions  $48 \times 48 \times 1$  for the magnetic anisotropy calculations.

### 2.5. Monte Carlo (MC) simulations

Solving the Heisenberg Spin Hamiltonian, considering localized spin moments, the  $T_C$  is computed by performing MC simulations:

$$H = - \sum_{i \neq j} J_{ij} \vec{e}_i \cdot \vec{e}_j - \sum_{i \neq j} \vec{D}_{ij} \cdot (\vec{e}_i \times \vec{e}_j) - \sum_{i \neq j} K_i (e_i^z)^2, \quad (4)$$

where  $J_{ij}$  and  $D_{ij}$  are isotropic symmetric and anti-symmetric interactions between  $i$ th and  $j$ th species,  $K_i$  is the single-ion anisotropy.

Classical MC simulations are performed via UppASD code [47] to estimate the magnetic ordering temperatures, where the calculated magnetic parameters are implemented in equation (6). Here, identical  $K_i$  was assumed for all Fe sites by averaging the total MAE/cell by the number of Fe atoms present in the unit cell. To achieve properly averaged properties, calculations are done for three ensembles in the supercell with size  $50 \times 50 \times 1$ , where periodic boundary conditions are imposed along the  $x$  and  $y$  axes.  $T_C$  is estimated by monitoring the cross sections of fourth-order cumulants of magnetization. The temperature is varied from 1000 K to 0 K in step of 5 K in the MC simulations. The number of MC steps considered in our calculations is  $1 \times 10^6$ .

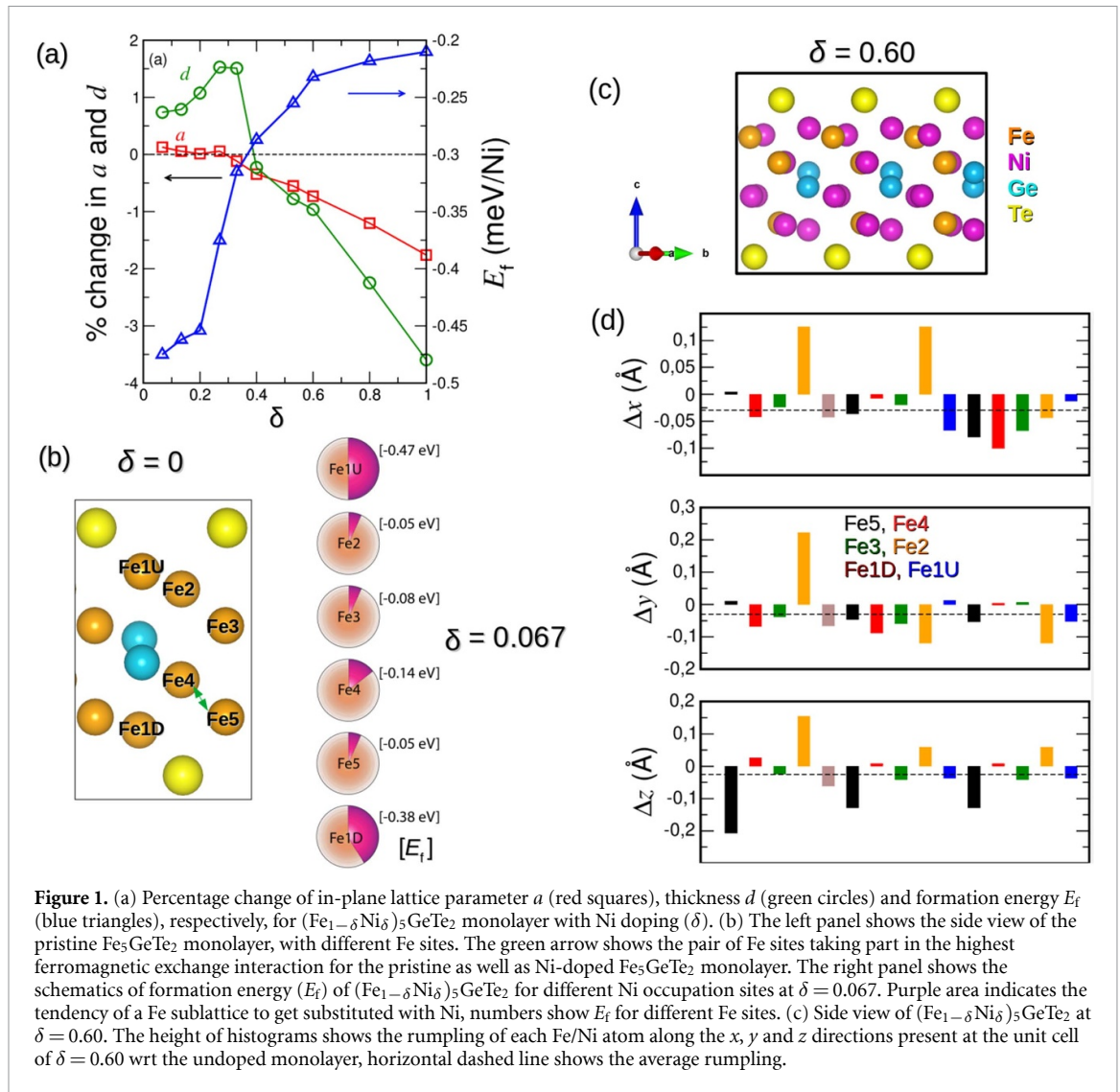


**Figure 1.** (a) Percentage change of in-plane lattice parameter  $a$  (red squares), thickness  $d$  (green circles) and formation energy  $E_f$  (blue triangles), respectively, for  $(\text{Fe}_{1-\delta}\text{Ni}_\delta)_5\text{GeTe}_2$  monolayer with Ni doping ( $\delta$ ). (b) The left panel shows the side view of the pristine  $\text{Fe}_5\text{GeTe}_2$  monolayer, with different Fe sites. The green arrow shows the pair of Fe sites taking part in the highest ferromagnetic exchange interaction for the pristine as well as Ni-doped  $\text{Fe}_5\text{GeTe}_2$  monolayer. The right panel shows the schematics of formation energy ( $E_f$ ) of  $(\text{Fe}_{1-\delta}\text{Ni}_\delta)_5\text{GeTe}_2$  for different Ni occupation sites at  $\delta = 0.067$ . Purple area indicates the tendency of a Fe sublattice to get substituted with Ni, numbers show  $E_f$  for different Fe sites. (c) Side view of  $(\text{Fe}_{1-\delta}\text{Ni}_\delta)_5\text{GeTe}_2$  at  $\delta = 0.60$ . The height of histograms shows the rumpling of each Fe/Ni atom along the  $x$ ,  $y$  and  $z$  directions present at the unit cell of  $\delta = 0.60$  wrt the undoped monolayer, horizontal dashed line shows the average rumpling.

### 3. Results and discussion

#### 3.1. Dopant induced structural modifications

The crystal structure of  $\text{Fe}_5\text{GeTe}_2$  is more complicated than other FGT systems. The structural peculiarities arise due to the presence of Fe1-Ge split sites, where Fe1 sublattice can occupy two possible sites, either directly above or below Ge [16, 26, 27]. The Fe1-Ge split sites in  $\text{Fe}_5\text{GeTe}_2$  can be incorporated by constructing a  $\sqrt{3} \times \sqrt{3}$  cell [27, 48]. From our previous DFT study, we found that  $\text{Fe}_5\text{GeTe}_2$  with Fe1-Ge splitting is energetically favored over the configuration without any splitting [16]. Therefore, a  $\sqrt{3} \times \sqrt{3}$  cell of  $\text{Fe}_5\text{GeTe}_2$  monolayer in up-down-up configuration of Fe atoms is considered in this study, where two (Fe1U) and one (Fe1D) Fe atoms are situated directly above and below Ge, respectively [16, 26, 27, 49]. We investigate the magnetic and electronic properties of the energetically favored configurations, determined by comparing the total energies of  $(\text{Fe}_{1-\delta}\text{Ni}_\delta)_5\text{GeTe}_2$  monolayers varying the position(s) of Ni dopant(s).

Our results show that the in-plane lattice parameter  $a$  remains almost unaltered compared to the

undoped system till  $\delta = 0.27$ , and starts to reduce when  $\delta > 0.30$ , see figure 1(a). However, the thickness  $d$  of the monolayer increases with doping up to  $\delta = 0.20$  but reduces for  $\delta \geq 0.40$  as shown in figure 1(a). Substitutional doping of Ni in  $\text{Fe}_5\text{GeTe}_2$  monolayer becomes energetically less favored with the increase in  $\delta$ . This is evident in figure 1(a) (blue triangles) where the formation energy  $E_f$  per Ni dopant is observed to increase with  $\delta$ . The formation energy  $E_f$  for Ni-doped  $\text{Fe}_5\text{GeTe}_2$  monolayer for a given doping  $\delta$  is given by:

$$E_f = E_{(\text{Fe}_{1-\delta}\text{Ni}_\delta)_5\text{GeTe}_2} - E_{\text{Fe}_5\text{GeTe}_2} + \delta E_{\text{Fe}} - \delta E_{\text{Ni}}, \quad (5)$$

where  $E_{(\text{Fe}_{1-\delta}\text{Ni}_\delta)_5\text{GeTe}_2}$ ,  $E_{\text{Fe}_5\text{GeTe}_2}$ ,  $E_{\text{Fe}}$  and  $E_{\text{Ni}}$  are the total energies for Ni-doped  $\text{Fe}_5\text{GeTe}_2$  monolayer, pristine  $\text{Fe}_5\text{GeTe}_2$  monolayer, bulk Fe and Ni crystals, respectively.

The left panel of figure 1(b) shows the side view of pristine  $\text{Fe}_5\text{GeTe}_2$  monolayer exhibiting different Fe sites. It is worth noting that during substitutional doping, the replacement of Fe1 species with Ni is energetically more favored than

other Fe sites. Between  $\delta = 0.067$  (Fe1U) and 0.20 (Fe1U+Fe1U+Fe1D) only Fe1 sublattice gets substituted by Ni. After Fe1, the next energetically favored occupation site for Ni dopant is Fe4. There is a significant increase in  $E_f$  between  $\delta = 0.20$  and 0.27, when one of the Fe4 atoms gets substituted together with Fe1U and Fe1D species. The presence of Ni causes an excess of electrons (figure S1 in supplementary information or SI), which might cause the lowering of  $E_f$ . For  $\delta \geq 0.33$ , Fe atoms belonging to other Fe sublattices (Fe2, Fe5 and Fe3) start to get substituted along with Fe1 and Fe4. Figure 1(b) shows how  $E_f$  varies when Ni substitutes different Fe sublattices at  $\delta = 0.067$ .

Structural distortion or rumpling (along  $x$ ,  $y$  and  $z$  directions) in the monolayer increases with Ni-doping (figure S1). Figure 1(c) shows the side view when  $\delta = 0.60$ . The height of the histograms in figure 1(d) shows the difference in  $x$ ,  $y$  and  $z$  coordinates between Fe or Ni atoms present in 0.60 Ni-doped and undoped systems for each (Ni/Fe) site of  $\sqrt{3} \times \sqrt{3}$  cell.  $\delta = 0.60$  causes significant rumpling of the atoms present at the sites of Fe5 (along  $z$ ) and Fe2 sublattices. A negative value of average rumpling (dashed horizontal line) supports the compression of cell parameters (both  $a$  and  $d$ ) with Ni doping, as we see in figure 1(a). It should be noted that [19] also finds a reduction in layer thickness with an increase in Ni doping. Apart from substitutional doping, Ni can occupy any vacant site of  $\sqrt{3} \times \sqrt{3}$  cell of  $\text{Fe}_5\text{GeTe}_2$ , including the vdW gap between different layers, such a scenario can occur in experiments performed at a finite temperature [19]. For example, in the  $\sqrt{3} \times \sqrt{3}$  cell, Ni can be placed at the position of missing Fe1, i.e. either below or above Ge. These indicate there are many degrees of freedom where Ni dopant can be located within the  $\text{Fe}_5\text{GeTe}_2$  system in reality.

### 3.2. Tuning of magnetism, exchange interactions and transition temperature

In our previous study, we showed that the inclusion of the dynamical electron correlation effect is an appropriate approach to determining the magnetic moment, exchange interactions and  $T_C$  of the  $\text{Fe}_n\text{GeTe}_2$  systems, compared to the standard GGA and GGA+U methods [17]. Therefore, we perform a charge self-consistent dynamical mean-field theory (DFT+DMFT) calculations as implemented in the FP-LMTO code RSPt [42, 43] to investigate the magnetic and electronic properties of  $(\text{Fe}_{1-\delta}\text{Ni}_\delta)_5\text{GeTe}_2$  monolayer.

Doping with Ni influences the magnetism of  $(\text{Fe}_{1-\delta}\text{Ni}_\delta)_5\text{GeTe}_2$  monolayer. The total spin moment  $M_{\text{tot}}$  reduces as a function of doping ( $\delta$ ). Figure 2(a) shows that  $M_{\text{tot}}$  decreases from  $10 \mu_B$  to  $0 \mu_B$  from  $\delta = 0$  to 1. These results are in good agreement with the saturation magnetic moment

of bulk  $(\text{Fe}_{1-\delta}\text{Ni}_\delta)_5\text{GeTe}_2$  [26]. Replacement of a single Fe1U with Ni causes a slight increase of the average moment  $M_{\text{tot}}^{\text{avg}} (= M_{\text{tot}}/\text{Fe}+\text{Ni})$ , see the red squares presented as the inset of figure 2(a). This happens because, in the case of pristine  $\text{Fe}_5\text{GeTe}_2$  monolayer, the moment of Fe1U species is  $-0.45 \mu_B$ , when one of the Fe1U gets replaced with Ni the remaining Fe1U gains  $1.48 \mu_B$  moment. Similar to  $M_{\text{tot}}$ ,  $M_{\text{tot}}^{\text{avg}}$  also reduces with an increase of doping concentration.

It is interesting to note that the direction of easy axis or magnetic anisotropy energy, MAE ( $= E_{\parallel} - E_{\perp}$ ) oscillates between in-plane and out-of-plane directions with  $\delta$ . However, for most of the doped systems, the easy axis lies in the  $xy$ -plane, see green squares presented as an inset in figure 2(a), which is in agreement with the experiment [19]. The strength of MAE for  $(\text{Fe}_{1-\delta}\text{Ni}_\delta)_5\text{GeTe}_2$  monolayers is much weaker than pristine  $\text{Fe}_3\text{GeTe}_2$  and  $\text{Fe}_4\text{GeTe}_2$  monolayers [17, 24]. The trend observed for MAE at lower  $\delta$  values can be correlated with the value of orbital moments obtained for different directions of spin axis [50], see table S2. It is worth noting that the switching of the easy axis is observed in Co-doped  $\text{Fe}_5\text{GeTe}_2$  with Co doping and electrical gating [28, 51]. Experiments report switching of easy axis for bulk  $\text{Fe}_5\text{GeTe}_2$  depending on the Fe concentration [26, 27]. Since the  $(\text{Fe}_{1-\delta}\text{Ni}_\delta)_5\text{GeTe}_2$  monolayers exhibit quite a weak MAE, the spin moments of these doped systems exhibit significant canting and noticeable spread of canting angles with respect to the easy axis, see figures S12 and S13 in SI. The average spin moment of Fe atoms first increases with doping, becomes maximum at  $\delta = 0.33$ , and then reduces, see figure 2(b). This happens due to the structural distortions in the unit cell of  $(\text{Fe}_{1-\delta}\text{Ni}_\delta)_5\text{GeTe}_2$  monolayer caused by the Ni dopant. Both the in-plane lattice parameter  $a$  and thickness  $d$  of the monolayer decrease as  $\delta \geq 0.4$ . Such reduction in the cell dimension is responsible for the decrease in the average magnetic moment of Fe. As we know the magnetic moment of Fe always reduces with a decrease in cell dimension and an increase in coordination number. Reduction at the moment is caused by the broadening of the density of states (DOS) as the atomic orbitals of the nearest neighbors (NNs) start to overlap [52, 53].

Similar to [19], our calculations also find that Ni dopants carry negligible spin moment (cyan squares in figure 2(b)) and are not responsible for the origin or tuning of ferromagnetism. The average orbital moment  $M_{\text{orb}}^{\text{avg}}$  of Fe remains between 0.05 and  $0.04 \mu_B$  till  $\delta = 0.80$ , see inset of figure 2(b). The orbital moment of Ni falls in the range of 0.01–0.02 and reduces for higher  $\delta$ .

We investigate how the isotropic symmetric ( $J_{ij}$ ) and antisymmetric ( $D_{ij}$ ) exchange interactions present in  $(\text{Fe}_{1-\delta}\text{Ni}_\delta)_5\text{GeTe}_2$  monolayer get modified

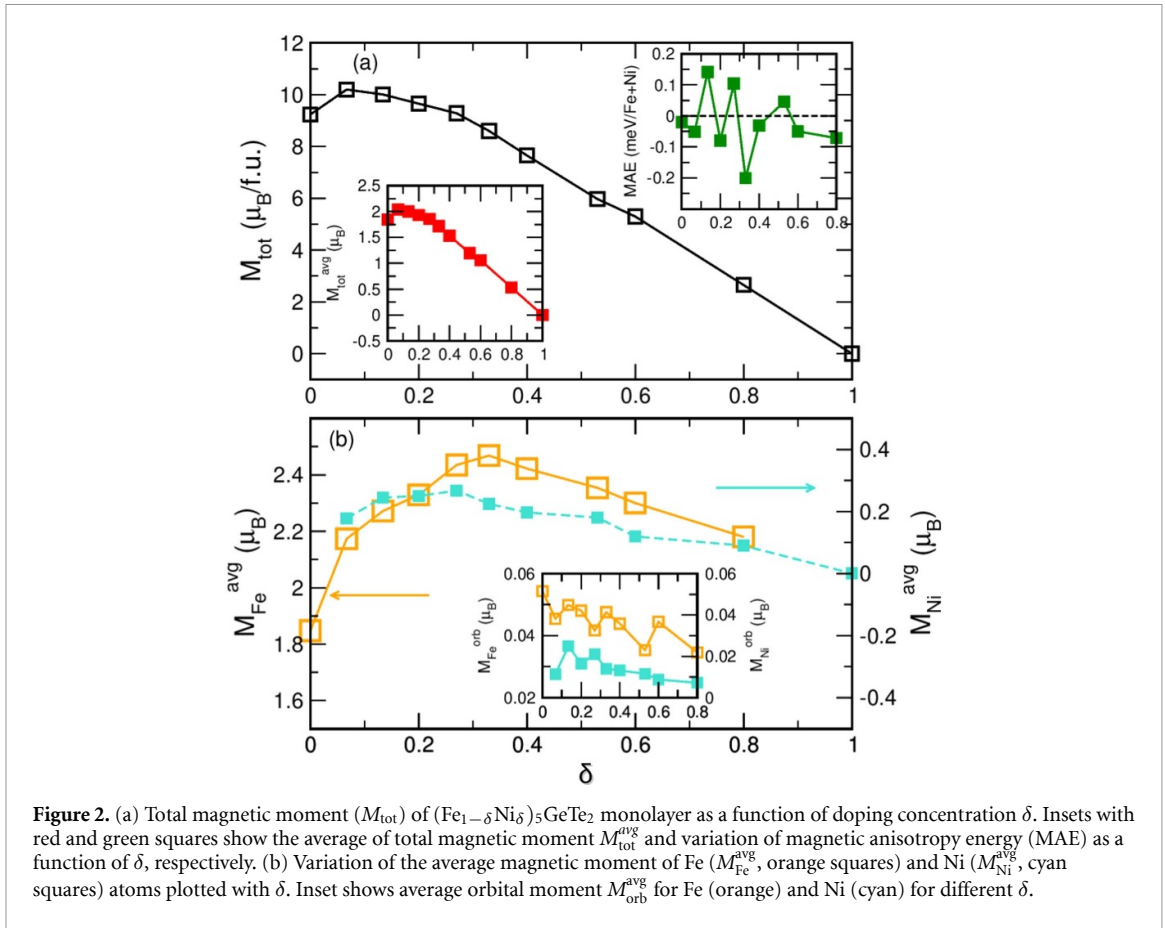


**Figure 2.** (a) Total magnetic moment ( $M_{\text{tot}}$ ) of  $(\text{Fe}_{1-\delta}\text{Ni}_\delta)_5\text{GeTe}_2$  monolayer as a function of doping concentration  $\delta$ . Insets with red and green squares show the average of total magnetic moment  $M_{\text{tot}}^{\text{avg}}$  and variation of magnetic anisotropy energy (MAE) as a function of  $\delta$ , respectively. (b) Variation of the average magnetic moment of Fe ( $M_{\text{Fe}}^{\text{avg}}$ , orange squares) and Ni ( $M_{\text{Ni}}^{\text{avg}}$ , cyan squares) atoms plotted with  $\delta$ . Inset shows average orbital moment  $M_{\text{orb}}^{\text{avg}}$  for Fe (orange) and Ni (cyan) for different  $\delta$ .

by varying  $\delta$ . Incorporating  $J_{ij}$ ,  $D_{ij}$  and MAE in the Heisenberg Spin-Hamiltonian:

$$H = - \sum_{i \neq j} J_{ij} \vec{e}_i \cdot \vec{e}_j - \sum_{i \neq j} \vec{D}_{ij} \cdot (\vec{e}_i \times \vec{e}_j) - \sum_{i \neq j} K_i (e_i^z)^2, \quad (6)$$

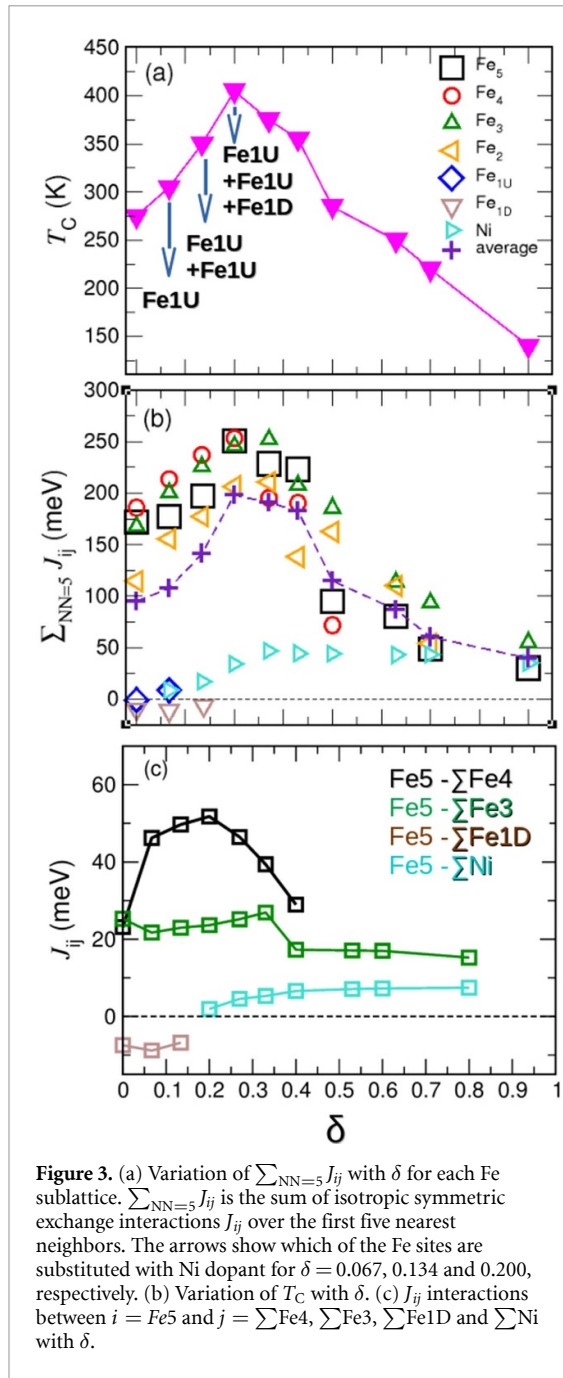
where  $J_{ij}$  and  $D_{ij}$  are the isotropic symmetric and antisymmetric exchange interactions between  $i$ th and  $j$ th species, respectively.  $K_i$  is the single-ion anisotropy energy for the  $i$ th site. The exchange interactions are calculated using DFT+DMFT technique. Similar to the pristine FGT systems, as reported in [17], in the case of Ni-doped  $\text{Fe}_5\text{GeTe}_2$  as well, we find that standard DFT or GGA significantly overestimates the isotropic symmetric exchange interactions or  $J_{ij}$  (see figure S8 in SI) and hence  $T_C$ , see table S3. Solving equation (6),  $T_C$  is obtained by MC simulations. Figure 3(a) shows there is a monotonic increase of  $T_C$  up to  $\delta = 0.20$ , then it reduces. Both the qualitative and quantitative trends of  $T_C$  vs.  $\delta$  plotted in figure 3 agrees well with the experimental report on bulk  $(\text{Fe}_{1-\delta}\text{Ni}_\delta)_5\text{GeTe}_2$  [19]. This again proves that the inclusion of the dynamic electron correlation effect is necessary to capture the correct magnetic behavior of the systems belonging to FGT family [17].

The critical  $\delta$  value at which  $T_C$  of the monolayer becomes maximum is not quantitatively exact as observed in the experiment. Such slight discrepancy

arises because in experiments, during the doping process, Ni can be placed at any vacant position present in the bulk system without replacing Fe, enhancing ferromagnetism and hence  $T_C$ . However, the rationale behind such a trend of  $T_C$  in  $(\text{Fe}_{1-\delta}\text{Ni}_\delta)_5\text{GeTe}_2$  is not addressed in the previous study.

Comparing the strength of different magnetic interactions we expect  $J_{ij}$  couplings must play the dominating role in determining  $T_C$ , in agreement with our study on pristine FGT systems [17]. To investigate the tuning of  $J_{ij}$  with  $\delta$ , we plot the  $J_{ij}$  values summed over the first five NNs for different  $i$ th Fe sublattices, see figure 3(b). We consider the number of NN up to 5, because the  $J_{ij}$  interactions decay significantly beyond that, see figures S4–S7 in SI. Most of the Fe sublattices show dominating FM  $J_{ij}$  interactions while Fe1D and Fe1U show antiferromagnetic (AFM) interactions, till  $\delta = 13.4\%$ .

The  $\sum_{\text{NN}=5} J_{ij}$  term for Fe5, Fe4, Fe3 and Fe2 first increases with  $\delta$ , becomes maximum for  $\delta = 0.20$ , then reduces for higher concentration.  $\sum_{\text{NN}=5} J_{ij}$  is plotted for each Fe species present in the  $\sqrt{3} \times \sqrt{3}$  cell. A monotonic increase of  $\sum_{\text{NN}=5} J_{ij}$  for each Fe sublattice (except Fe1U and Fe1D) is observed up to  $\delta = 0.20$ . This happens because till  $\delta = 0.20$ , except Fe1, the number of Fe sublattices present in the unit cell remains 3. For  $\delta > 0.20$  the Fe atoms belonging to Fe4 sublattice start to get substituted in addition with Fe1U and Fe1D, as we see in figure 1(d). The

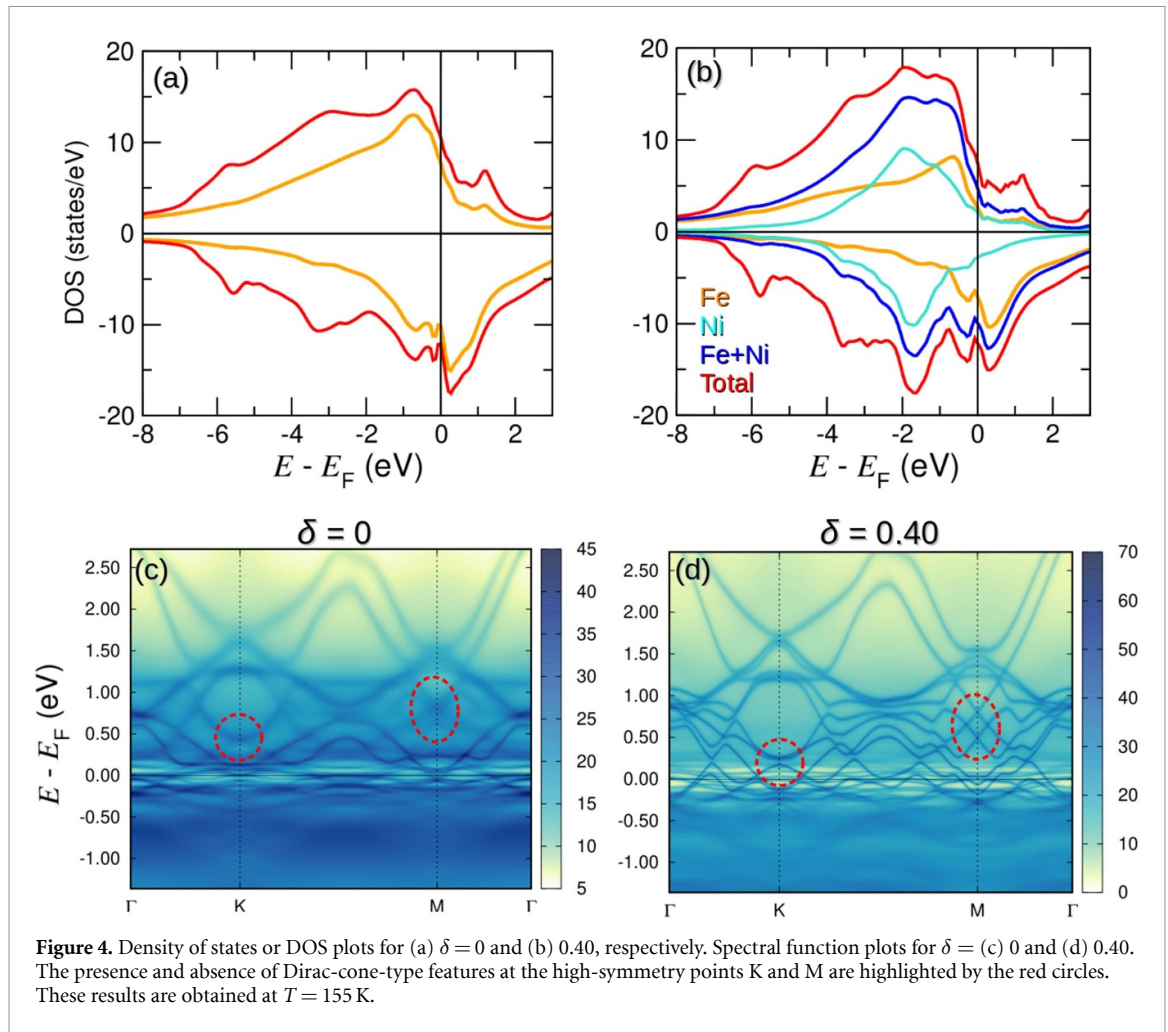


replacement of magnetic Fe causes sharp reduction in  $\sum_{NN=5} J_{ij}$  of Fe4 for  $\delta > 0.20$ . After 0.40, all three Fe4 atoms get substituted with Ni, see red circles in figure 3(a). The gradual replacement of different Fe sublattices with Ni causes rapid lowering in  $\sum_{NN=5} J_{ij}$  for  $\delta \geq 0.33$ . In addition to possessing negligible magnetic moment (figure 2), Ni dopants have a negligible contribution to the  $J_{ij}$  interactions. The magnitude of  $\sum_{NN=5} J_{ij}$  for Ni is  $\sim 10$  times smaller than the Fe sublattices for  $\delta \leq 0.20$ . As the number of Ni atoms present in  $(\text{Fe}_{1-\delta}\text{Ni}_\delta)_5\text{GeTe}_2$  increases with  $\delta$ ,  $\sum_{NN=5} J_{ij}$  for Ni becomes comparable with Fe for  $\delta \geq 0.60$ . For  $i = \text{Ni}$ , non-zero exchange couplings exist when  $j = \text{Fe}$ , otherwise, interactions between Ni themselves are rather weak. The violet symbols show the average variation of  $\sum_{NN=5} J_{ij}$  with Ni doping,

which increases from 0 to 0.20 and then reduces. The same investigation has been made for  $D_{ij}$  interactions as well. For a given  $\delta$ , the magnitude of  $\sum_{NN=5} D_{ij}$  for any  $i$ th Fe species is  $\sim 10$  times smaller than  $\sum_{NN=5} J_{ij}$  (figure S9 in SI).

In our previous study, we find that the dominating first NN exchange interaction exists between Fe5 and Fe4 in the pristine  $\text{Fe}_5\text{GeTe}_2$  monolayer [17]. Further analysis of  $J_{ij}$  couplings among individual Fe pairs reveals that in the case of Ni-doped  $\text{Fe}_5\text{GeTe}_2$  monolayer as well the couplings between Fe5 and Fe4 play the dominating role. Figure 3(c) shows  $J_{ij}$  interactions when  $i = \text{Fe5}$  and  $j$ th species are considered to be the NNs of Fe5, i.e. Fe4, Fe3, Fe1D and Ni. We find, among these neighbors, exchange couplings between Fe5– $\sum \text{Fe4}$  vary significantly with doping and tune the  $T_C$ . The  $J_{ij}$  interaction between Fe5 and Fe4 increases with  $\delta$  and then reduces for  $\delta \geq 0.27$ . The increase of  $J_{54}$  up to  $\delta = 0.20$  occurs due to the following reasons: (i) reduction of Fe5–Fe4 bond length with  $\delta$  (figure S2 in SI), (ii) among the first five NNs of Fe5, three of them are Fe4 species with the strongest FM coupling. Therefore,  $J_{54} = (J_{54_1} + J_{54_2} + J_{54_3})$  for  $\delta \leq 0.20$ . The reduction in  $J_{54}$  for  $\delta > 0.20$  occurs due to the gradual replacement of Fe4 with Ni, causing a decrease in the number of Fe4 belonging to the first five NN of Fe5, see figure S3 in SI for details. No particular trend is observed for  $J_{53}$  (green squares), up to  $\delta = 0.60$ .  $J_{ij}$  exchange interactions between Fe5 and Fe1D is AFM (brown squares), and replacement of Fe1D with Ni triggers FM exchange coupling (cyan squares). Comparing different  $J_{5j}$  interactions we see  $J_{54}$  follows the similar trend as  $\sum_{NN=5} J_{5j}$  (black squares) and average of  $\sum_{NN=5} J_{ij}$  (purple symbols) in figure 3(b). Therefore,  $J_{54}$  has a major influence on  $T_C$ , especially for  $\delta \leq 0.20$ . From figures 3(a)–(c) we can establish the fact that the strength of  $J_{ij}$  interactions between any particular pair of magnetic atoms mainly depends on the NN distance and the effective coordination number, which tunes the  $T_C$  of a system.

We check the robustness of the magnetic properties, e.g. magnetic moment, exchange interactions, magnetic anisotropy and  $T_C$  varying the average  $U_{\text{eff}}^{\text{avg}}$ . Our results show that the maximum uncertainty in the magnetic moment, isotropic symmetric exchange interactions and magnetic anisotropy is  $\sim 1\%$ ,  $\sim 12\%$  and  $\sim 15\%$ , respectively, within a reasonable range of  $U_{\text{eff}}^{\text{avg}}$  for Fe-3d, i.e. from 3.5 eV to 5 eV.  $T_C$  varies between 400 K and 350 K as  $U_{\text{eff}}$  varies between the cLR-calculated different Fe sublattice-projected values and 5 eV. Though there is 12.5% difference in the  $T_C$  value, the relative trend of  $T_C$  vs.  $\delta$  should remain unchanged with a change in  $U_{\text{eff}}$  within this range. This happens because the nature (FM/AFM) of the  $J_{ij}$  couplings for a given  $\delta$  does not change as  $U_{\text{eff}}$  varies within a reasonable range and since the  $J_{ij}$  interactions play the dominating role in determining  $T_C$ , one should expect similar variation in  $T_C$  with  $\delta$  for



different  $U_{\text{eff}}$ . The magnetic properties obtained for different  $U_{\text{eff}}$  values are reported in tables III–V, and figures S21–S23 in the SI. Previous studies on FGT systems show the reasonable choice for the effective Hubbard  $U$  parameter or  $U_{\text{eff}}$  should be  $\sim 4$  eV [54], which is close to the Fe-site-specific  $U_{\text{eff}}$  values we calculate from the cLR method.

### 3.3. Modifications in spectral properties and electron correlation

Next, we discuss how substitutional doping modifies the electronic structure of  $(\text{Fe}_{1-\delta}\text{Ni}_\delta)_5\text{GeTe}_2$ . Figures 4(a) and (b) show the DOS for  $\delta = 0$  and 0.40, respectively (see figure S16 in SI for details). The intensity of DOS projected on Fe atoms reduces with Ni doping. More importantly, the Fe states have a dominating contribution close to  $E_F$ , the maximum intensity of Ni states arises away from  $E_F$ .

Figures 4(a) and (b) show the spectral function  $A(k, \omega)$  for  $\delta = 0$  and 0.40, respectively. The main differences observed in  $A(k, \omega)$  as a function of  $\delta$  are: (i) the smearing-width or broadening of energy levels reduces and they become sharper (intensity increases) as  $\delta$  increases. This happens due to the decrease in electron correlation effect causing the increase in quasi-particle lifetime. (ii) Presence of

Dirac-cone-type feature at the high-symmetry point K for  $\delta = 0$ , which gradually disappears with an increase in  $\delta$ . (iii) Multiple well-separated Dirac cones appear for  $\delta = 0.40$  at the high-symmetry point M due to splitting between energy levels. The main contribution to such Dirac-cone-type features comes from the Fe- $d$  states. Further analysis shows the structural distortions induced by the presence of Ni dopant in  $\text{Fe}_5\text{GeTe}_2$  are responsible for such modifications in the energy dispersion, see SI. The gradual change in the spectral function with Ni doping is shown in figure S15 in SI.

Similar to other FGT systems, the admixture of localized and itinerant electrons exists in  $\text{Fe}_5\text{GeTe}_2$  as well [17, 33]. The effective mass  $(m^*/m)_{l\sigma}$  provides the quantitative measurements of electronic correlation [55].

$$(m^*/m)_{l\sigma} = \left( 1 - \frac{\delta \text{Re}\Sigma_{l\sigma}(\omega)}{\delta\omega} \Big|_{\omega=0} \right), \quad (7)$$

where  $\text{Re}\Sigma(\omega)$  is the real-part of self-energy with real frequency  $\omega$  (see figures S19 and S20) and  $\sigma$  is electron spin. Both the qualitative and quantitative trends of  $m^*/m$  with  $\delta$  remain almost unaltered for different Fe- $d$  states.  $m^*/m$  for the majority spin channel of  $d_{z^2}$  and  $d_{xy}$  are plotted in figures 5(a) and (b), (see

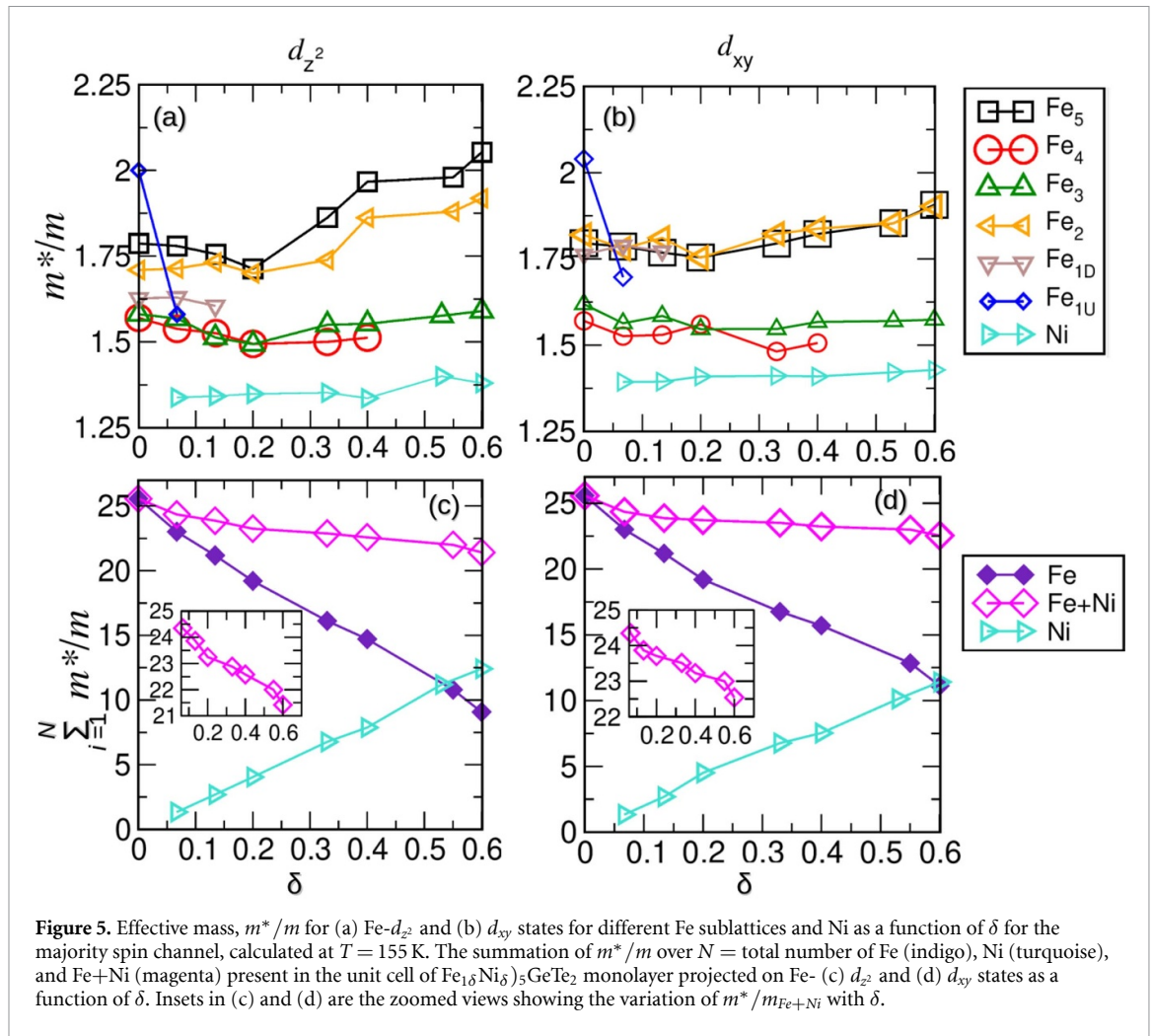


figure S18 for other  $Fe-d$  states). The enhancement of effective mass quantifies how much the  $Fe-d$  electrons effectively become heavier because of electron correlation. For the pristine  $Fe_5GeTe_2$  monolayer, the  $Fe_{1U}$  site exhibits the highest electron correlation with the largest value of  $m^*/m$ . There is a slight reduction in effective mass between  $\delta = 0$  and  $0.20$ , then it increases for  $\delta > 0.20$ , especially in the case of  $Fe_5$  and  $Fe_2$ . The values of  $(m^*/m)_{l\sigma}$  are larger for  $Fe_5$  and  $Fe_2$  sublattices than  $Fe_3$  and  $Fe_4$  species. This implies the  $d$  electrons belonging to  $Fe_5$  and  $Fe_2$  sublattices are more correlated than  $Fe_3$  and  $Fe_4$ . More interestingly, the  $Fe_{1U}$  species has the highest  $m^*/m$  at  $\delta = 0$ , then it reduces with Ni doping. The sub-lattice categorization of pristine  $Fe_5GeTe_2$  monolayer in terms of structural, magnetic and electronic properties are already discussed in [16, 17]. The enhancement in  $m^*/m$  for  $Fe_5$  and  $Fe_2$  occurs due to the narrowing of the  $Fe d$ -bands close to the Fermi energy, see figure S18. Interestingly, site dependence of  $m^*/m$  is observed for both the pristine and doped  $Fe_5GeTe_2$  systems. Similar to  $(Fe_{1-\delta}Ni_{\delta})_5GeTe_2$ , site-dependent electron correlation is present in  $Fe_3GeTe_2$  as well [32]. It is important to note that the effective mass of Ni- $d$  is

lower than  $Fe-d$ , signifying the Ni- $d$  states are less correlated or more delocalized around the Fermi level than  $Fe-d$  (see figure S16). Though the effective mass of a single Fe atom belonging to the  $Fe_5$  and  $Fe_2$  sublattices increases with  $\delta$ , the total effective mass of Fe atoms, i.e.  $\sum_i^N (m^*/m)_{Fe}$ , where  $N$  is the number of Fe atoms present in the unit cell, reduces with  $\delta$ , see the indigo symbols in figures 5(c) and (d). While the effective mass sum over the Ni atoms present in the unit cell,  $\sum_i^N (m^*/m)_{Ni}$ , increases with  $\delta$ , see turquoise symbols in figures 5(c) and (d). Note, the maximum value of  $\sum_i^N (m^*/m)_{Fe} \approx 2 \times \sum_i^N (m^*/m)_{Ni}$ . However, the total effective mass  $\sum_i^N (m^*/m)_{Fe+Ni}$  of Fe+Ni decreases with  $\delta$ , see magenta symbols in figures 5(c) and (d). These results confirm that the strength of electron correlation reduces with  $\delta$  in  $(Fe_{1-\delta}Ni_{\delta})_5GeTe_2$ .

#### 4. Conclusions

In summary, we investigated how the structural modifications caused by substitutional doping with Ni can tune the exchange interactions in  $Fe_5GeTe_2$ , which is responsible for achieving ferromagnetism

beyond room temperature. Using the  $\sqrt{3} \times \sqrt{3}$  cell of  $(\text{Fe}_{1-\delta}\text{Ni}_\delta)_5\text{GeTe}_2$  monolayer, we find the dynamic electron correlation plays a crucial role in correctly describing the magnetic behavior of the Ni-doped system. Our results show that  $T_C$  of the monolayer increases up to  $\sim 400$  K by substitutional doping with Ni. The variation in  $T_C$  for  $(\text{Fe}_{1-\delta}\text{Ni}_\delta)_5\text{GeTe}_2$  monolayer with  $\delta$  is in good agreement with a recent experimental report on bulk  $(\text{Fe}_{1-\delta}\text{Ni}_\delta)_5\text{GeTe}_2$ . We identify the isotropic symmetric exchange interactions are the dominating mechanisms to govern  $T_C$ . Moreover, coupling between Fe5 and Fe4 is mainly responsible for the observed trend in  $T_C$  with Ni doping. FM interactions present in  $(\text{Fe}_{1-\delta}\text{Ni}_\delta)_5\text{GeTe}_2$  get maximized at  $\delta = 0.20$ , causing the highest value of transition temperature. Our results show that the structural modifications caused by the Ni dopant, modify the NN distances and effective coordination numbers, which affect the dominating exchange couplings. Our study also shows how Ni-doping influences the spectral features and site-dependent effective masses arising from electron correlation. We also unveil the microscopic mechanisms responsible for the increase in  $T_C$  at lower doping and explain why it decreases with an increase in Ni concentration. Apart from magnetic properties, this work also sheds light on how the sublattice-specific electron correlation effect varies with Ni doping. Overall, this study not only clarifies the unconventional  $T_C$  vs. doping behavior first observed in experiments by Chen *et al* [19], but also should guide the community on how to control magnetic transition and tune  $T_C$  for similar systems by introducing external factors, for example, chemical impurities or substitutional doping.

### Data availability statement

All data that support the findings of this study are included within the article (and any supplementary files).

### Acknowledgments

B S and S G acknowledge a postdoctoral grant from Carl Tryggers Stiftelse (CTS 20:378). B S acknowledges financial support from Swedish Research Council (Grant No. 2022-04309). The computations were enabled by resources provided by the National Academic Infrastructure for Supercomputing in Sweden (NAISS) at UPPMAX (NAISS 2023/5-238) and the Swedish National Infrastructure for Computing (SNIC) (SNIC 2022/3-30) at NSC and PDC partially funded by the Swedish Research Council through Grant Agreement Nos. 2022-06725 and 2018-05973. B S and S E also acknowledge the allocation of supercomputing hours in EuroHPC resources in Karolinska supercomputer (EU2022D10-059, EU2022D11-001) in the Czech Republic and

LUMI supercomputer (EHPC-DEV-2022D10-059, EHPC-DEV-2022D10-057) in Finland.

### ORCID iDs

Sukanya Ghosh  <https://orcid.org/0000-0002-6204-5760>

Biplab Sanyal  <https://orcid.org/0000-0002-3687-4223>

### References

- [1] Gibertini M, Koperski M, Morpurgo A F and Novoselov K S 2019 *Nat. Nanotechnol.* **14** 408–19
- [2] Gong C and Zhang X 2019 *Science* **363** eaav4450
- [3] Mermin N D and Wagner H 1966 *Phys. Rev. Lett.* **17** 1133–6
- [4] Jenkins S, Rózsa L, Atxitia U, Evans R F L, Novoselov K S and Santos E J G 2022 *Nat. Commun.* **13** 6917
- [5] Zollner K, Gmitra M and Fabian J 2020 *Phys. Rev. Lett.* **125** 196402
- [6] Zhu W, Song C, Han L, Guo T, Bai H and Pan F 2022 *Nat. Commun.* **13** 6428
- [7] Verzhbitskiy I A, Kurebayashi H, Cheng H, Zhou J, Khan S, Feng Y P and Eda G 2020 *Nat. Electron.* **3** 460–5
- [8] Lee I, Utermohlen F G, Weber D, Hwang K, Zhang C, van Tol J, Goldberger J E, Trivedi N and Hammel P C 2020 *Phys. Rev. Lett.* **124** 017201
- [9] Wang C, Gao Y, Lv H, Xu X and Xiao D 2020 *Phys. Rev. Lett.* **125** 247201
- [10] Jiang S, Li L, Wang Z, Mak K F and Shan J 2018 *Nat. Nanotech.* **13** 549–53
- [11] Ghosh S, Stojić N and Binggeli N 2021 *Nanoscale* **13** 9391–401
- [12] Ghosh S, Stojić N and Binggeli N 2019 *Physica B* **570** 166–71
- [13] Sun X *et al* 2020 *Nano Res.* **13** 3358–63
- [14] Burch K S, Mandrus D and Park J-G 2018 *Nature* **563** 47–52
- [15] Wang N *et al* 2019 *J. Am. Chem. Soc.* **141** 17166–73
- [16] Ershadrad S, Ghosh S, Wang D, Kvashnin Y and Sanyal B 2022 *J. Phys. Chem. Lett.* **13** 4877–83
- [17] Ghosh S, Ershadrad S, Borisov V and Sanyal B 2023 *npj Comput. Mater.* **9** 86
- [18] Seo J *et al* 2020 *Sci. Adv.* **6** 8912
- [19] Chen X *et al* 2022 *Phys. Rev. Lett.* **128** 217203
- [20] Zhao B *et al* 2023 *Adv. Mater.* **35** 2209113
- [21] Hu X, Zhao Y, Shen X, Krashennnikov A V and Chen Z 2020 *ACS Appl. Mater. Interfaces* **12** 26367–73
- [22] Zhu M, You Y, Xu G, Tang J, Gong Y and Xu F 2021 *Intermetallics* **131** 107085
- [23] Deng Y *et al* 2018 *Nature* **563** 94–99
- [24] Kim D, Lee C, Jang B G, Kim K and Shim J H 2021 *Sci. Rep.* **11** 17567
- [25] Weber D, Trout A H, McComb D W and Goldberger J E 2019 *Nano Lett.* **19** 5031–5
- [26] Zhang H *et al* 2020 *Phys. Rev. B* **102** 064417
- [27] May A F, Ovchinnikov D, Zheng Q, Hermann R, Calder S, Huang B, Fei Z, Liu Y, Xu X and McGuire M A 2019 *ACS Nano* **13** 4436–42
- [28] May A F, Du M-H, Cooper V R and McGuire M A 2020 *Phys. Rev. Mater.* **4** 074008
- [29] Zhang H *et al* 2022 *Phys. Rev. Mater.* **6** 044403
- [30] Zhang H *et al* 2022 *Sci. Adv.* **8** eabm7103
- [31] Tian C, Pan F, Xu S, Ai K, Xia T and Cheng P 2020 *Appl. Phys. Lett.* **116** 202402
- [32] Kim T J, Ryee S and Han M J 2022 *npj Comput. Mater.* **8** 245
- [33] Zhao M *et al* 2021 *Nano Lett.* **21** 6117–23
- [34] Zhang Y *et al* 2018 *Sci. Adv.* **4** eaao6791
- [35] Wang B *et al* 2023 *Appl. Phys. Lett.* **123** 071902
- [36] Hu X, Yao D-X and Cao K 2022 *Phys. Rev. B* **106** 224423
- [37] Kresse G and Joubert D 1999 *Phys. Rev. B* **59** 1758
- [38] Kresse G and Hafner J 1994 *J. Phys.: Condens. Matter* **6** 8245

- [39] Perdew J P, Burke K and Ernzerhof M 1996 *Phys. Rev. Lett.* **77** 3865
- [40] Monkhorst H J and Pack J D 1976 *Phys. Rev. B* **13** 5188
- [41] Georges A, Kotliar G, Krauth W and Rozenberg M J 1996 *Rev. Mod. Phys.* **68** 13–125
- [42] Wills J, Eriksson O, Alouani M and Price D 2000 *Full-Potential LMTO Total Energy and Force Calculations* (Springer)
- [43] Grånäs O, Di Marco I, Thunström P, Nordström L, Eriksson O, Björkman T and Wills J 2012 *Comput. Mater. Sci.* **55** 295–302
- [44] Purovskii L V, Katsnelson M I and Lichtenstein A I 2005 *Phys. Rev. B* **72** 115106
- [45] Kvashnin Y O, Grånäs O, Di Marco I, Katsnelson M I, Lichtenstein A I and Eriksson O 2015 *Phys. Rev. B* **91** 125133
- [46] Borisov V et al 2022 *Phys. Rev. Mater.* **6** 084401
- [47] Eriksson O, Bergman A, Bergqvist L and Hellsvik J 2017 *Atomistic Spin Dynamics: Foundations and Applications* (Oxford University Press)
- [48] Ly T T et al 2021 *Adv. Funct. Mater.* **31** 2009758
- [49] May A F, Bridges C A and McGuire M A 2019 *Phys. Rev. Mater.* **3** 104401
- [50] Bruno P 1989 *Phys. Rev. B* **39** 865–8
- [51] Tang M 2023 *Nat. Electron.* **6** 28–36
- [52] Desjonquères M-C, Barreteau C, Autès G and Spanjaard D 2007 *Phys. Rev. B* **76** 024412
- [53] Liu F, Khanna S N and Jena P 1990 *J. Appl. Phys.* **67** 4484–6
- [54] Shen Z-X, Bo X, Cao K, Wan X and He L 2021 *Phys. Rev. B* **103** 085102
- [55] Ramšak A, Horsch P and Fulde P 1992 *Phys. Rev. B* **46** 14305–8